RESEARCH ARTICLE | DECEMBER 11 2024

Coherence mode and Floquet analysis on flow past a rectangular cylinder with small angle of attack

Lingyu Qiao (乔凌宇); Ying Zhao (赵颖); Lei Zhou (周蕾); Yifeng Ai (艾轶峰); Qingchi Zhu (朱清驰);
Hongfu Zhang (张洪福)

Physics of Fluids 36, 123616 (2024)
https://doi.org/10.1063/5.0241201

Physics of Fluids ARTICLE pubs.aip.org/aip/pof

Coherence mode and Floquet analysis on flow past a rectangular cylinder with small angle of attack

Cite as: Phys. Fluids **36**, 123616 (2024); doi: 10.1063/5.0241201
Submitted: 29 September 2024 · Accepted: 1 November 2024 ·
Published Online: 11 December 2024

Lingyu Qiao (乔凌宇),[1] Ying Zhao (赵颖),[1,a)] Lei Zhou (周蕾),[2,3] Yifeng Ai (艾轶峰),[4] Qingchi Zhu (朱清驰),[1] and Hongfu Zhang (张洪福)[1,a)]

AFFILIATIONS

[1]School of Civil Engineering and Transportation, Northeast Forestry University, Harbin 150040, China
[2]Department of Civil Engineering, Hong Kong Polytechnic University, Hong Kong, China
[3]School of Civil Engineering, Central South University, Changsha 410083, China
[4]Architecture and Civil Engineering Department, City University of Hong Kong, Tat Chee Avenue No. 83, Kowloon, Hong Kong, China

[a)]Authors to whom correspondence should be addressed: zhaoyinglxd@nefu.edu.cn and zhanghongfu@nefu.edu.cn

ABSTRACT

This paper focuses on a typical bluff body, a rectangular cylinder with an aspect ratio of 5, and quantitatively analyzes the fluid force coefficients and Strouhal number (*St*) under different angles of attack (α) and Reynolds numbers (*Re*) through numerical simulations. The higher-order dynamic mode decomposition method is used for coherence mode analysis, and Floquet instability analysis is used to identify the 3D transitional angle of attack (α_{3D}) at different *Re* as well as the Floquet modes at various α. The results show that increasing the angle of attack significantly raises the mean drag coefficient ($\bar{C}_D$) and fluctuating lift coefficient (C'_L), while the *St* number gradually decreases. This leads to the emergence of vortices and complex flow structures of different scales and frequencies at the rear edge of the rectangular cylinder and its lower cavity region, accompanied by increased downstream turbulence intensity. Furthermore, the 3D transitional angle of attack (α_{3D}) decreases with increasing *Re*. Two types of Floquet modes are identified within the range of *Re* and α, namely, Mode A and Quasi-Periodic Mode QP. This study provides important insights and theoretical support for a deeper understanding of flow evolution problems.

I. INTRODUCTION

A rectangular cylinder is a typical rectangular blunt body that provides a wide range of types of flow characteristics and vortex dynamics behavior based on the aspect ratio (*AR*: the ratio of the long side to the short side) and thus can be used to study complex flow and aerodynamic mechanisms.[1] Unlike the typical cylindrical winding vortex shedding mode, Nakamura *et al.*[2,3] found that collisional shear layer instability is the main cause of vortex excitation in rectangular blunt bodies. Nowadays, $AR = 5$ rectangular cylinders have received much attention in many engineering fields such as buildings, bridge main girders, signal towers, etc., both in basic research and practical applications, because of their representativeness. The benchmark problem study on the aerodynamic performance of rectangular cross-section beams with $AR = 5$ was initiated in the Sixth International Symposium on Blunt Body Aerodynamics and Applications in 2008, or BARC for short.[4] Subsequently, many scholars have investigated various flow and aerodynamic performances of rectangular sections with $AR = 5$. Bruno analyzed fluid separation and reattachment around a fixed rectangular cylinder with $AR = 5$ at high *Re*, starting from the orthogonal decomposition and coherence function of the fluctuating pressure field on the lateral surface.[5] Zhu *et al.*[6,7] studied and analyzed the flow characteristics of a rectangular cylinder with $AR = 5$ at low α and low *Re*. They observed that as *Re* increased from 100 to 300, the flow structure gradually transitioned from laminar to turbulent, and at the same time, the kinetic energy of the fluid at the trailing edge increased, along with an increase in the degree of nonlinearity in the dynamical system. Scholars have also conducted in-depth studies on the effect of *Re* on the wraparound flow of rectangular cylinders,[8] the relationship between different height-to-width ratios of the cross section and flow-induced vibrations,[9] as well as the distribution and correlation of surface pressure around the cross section.[10]

The visualization of flow structures in a flow field not only helps in understanding and optimizing flow phenomena but also has applications in aerodynamic design, structural safety assessment, and other areas. However, observing the subtle and underlying changes in flow structures can be challenging. The dynamic mode decomposition (DMD) method, based on Koopman theory, addresses these challenges by reducing the dimensionality of high-dimensional nonlinear dynamical systems. This method extracts valuable dynamic information and key dynamic modes, reflecting the main characteristics and evolution of flow in complex flow field data, and can be used for flow prediction and control.[11–13] However, classical DMD methods may encounter numerical stability issues in some cases, especially when dealing with large-scale data or long time series. In such situations, unstable or misleading modes may be extracted. Clainche *et al.* addressed this by integrating the delayed embedding theory of Takens with classical DMD to develop higher-order dynamic mode decomposition (HODMD),[14,15] HODMD can improve frequency resolution by extending the time dimension of the data matrix, thereby capturing both low and high-frequency components of the flow more accurately. Additionally, it is more robust to noise and better handles data with noise.[16,17]

After passing through a blunt body, the fluid not only forms a spanwise vortex shed in the wake region but also generates a streamwise vortex attached to the spanwise vortex, which then leads to the formation of turbulence.[18,19] This phenomenon, which exhibits specific 3D features, is defined as secondary wake instability, also known as 3D instability. The transition from a 2D to a 3D wake needs to be studied in depth, as the forces acting on the object may change with the development of the 3D structure in the wake, potentially harming the object or the surrounding environment. Barkley *et al.* found that the wake transition mechanism in cylinders involves two different scales of 3D instability modes, namely Mode A and Mode B, which occur within different ranges of *Re*.[20] Floquet instability analysis by Leblanc and Godeferd showed that the value of the streamwise velocity contours of Mode A is primarily concentrated in the spanwise vortex core, whereas those of Mode B is more concentrated in the braid region.[21] Lin *et al.*[22] explored the inherent physical connection of vorticity between Modes A and B during the 3D wake transition, determined the characteristics of the vertical vorticity for both modes and found that the vortex pattern in each mode represents a fundamental vortex structure. Additionally, two different modes, the subharmonic Mode C[23,24] and the quasi-periodic Mode QP,[25,26] have been shown to exist in more blunt body shapes. Rao *et al.*[27] discovered that after the spatiotemporal symmetry of the blunt body wake is disrupted, Mode C can emerge due to localized flow acceleration on one side of the blunt body. Park and Yang[28] performed Floquet analysis on cylinders and found that the effect of planar shear on 3D instability varies with the type of 3D instability. Specifically, the flow asymmetry induced by planar shear suppresses Mode QP but generates Mode C, while Modes A and B are stabilized by planar shear. Conversely, Mode C is strengthened with increasing shear. However, the cylindrical transition phenomenon is not universally applicable, and as Ryan points out in his article,[29] the relevant studies on blunt bodies still need to be further explored. Many scholars have studied the tail flow region of blunt bodies in different shapes and states, such as flat plates,[30] flat plates with elliptical leading edges,[31] square cylinders with different angles of incidence, and square cylinders in tandem,[32,33] oscillating cylinders, and square cylinder.[34,35] These 3D instability modes have been studied in depth playing an important role in engineering applications in the fields of drag reduction and flow control.

Therefore, in this study, numerical simulation, HODMD, and Floquet analysis of the flow around a rectangular cylinder with an aspect ratio of five are carried out, and the results are divided into two parts. The first part investigates the effect of the variation of α on the 2D flow around the rectangular cylinder. α values of 0°, 2°, 4°, 6°, 8°, 10°, 12°, and 15° as well as *Re* values of 200, 250, and 300 are considered. The α values selected for the HODMD analysis are 0°, 10°, and 15°, with a *Re* value of 300. The second part explores the effect of increasing the angle of attack on the tail flow around the rectangular cylinder, transitioning from 2D to 3D development. Additionally, it plots the behavior of the Floquet multiplier as a function of α and the number of spanwise waves.

Section II of this paper will describe the simulation methodology, flow field setup, and details of the HODMD and Floquet methods. Section III will cover the validation of the simulation methodology. Section IV will quantitatively analyze the fluid force coefficients and Strouhal number, perform modal analyses of flow field vorticity and pressure using the HODMD method, and identify the 2D to 3D flow transition and different 3D instability modes that emerge with changes in α through Floquet instability analysis. The conclusions of the study will be summarized in Sec. V.

II. COMPUTATIONAL METHOD

A. Base flow

For the flow problem around an $AR = 5$ rectangular cylinder at different α, the governing equations are the continuity equation and the incompressible Navier–Stokes equation. When expressed in dimensionless form, these equations are

$$\nabla \cdot U = 0, \tag{1}$$

$$\frac{\partial U}{\partial t} = -(U \cdot \nabla)U - \nabla P + \frac{1}{Re}\nabla^2 U + S. \tag{2}$$

Here, P represents pressure, U is the 2D velocity vector, and t represents time. We used the high-order spectral-element open-source code Nektar++[36] to solve these equations and the Galerkin spectral-element method to determine the periodic 2D flow field. The spatial domain is discretized, within each cell, where the solution variables are represented using sixth-order interpolated Lagrange polynomial shape functions. The inlet length, symmetry boundary width, and outlet length are shown in Fig. 1. At the inlet, upper, and lower side of the computational domain, free-stream boundary conditions (Dirichlet boundary conditions) were applied. At the outlet boundary, a pressure outlet condition with zero static gauge pressure was applied. In addition, D represents the width of the rectangular cylinder, and U_0 represents the inlet flow velocity, which is 1 m/s. The rectangular cylinder is fixed with an adjustable inclination angle, allowing for variation in α of

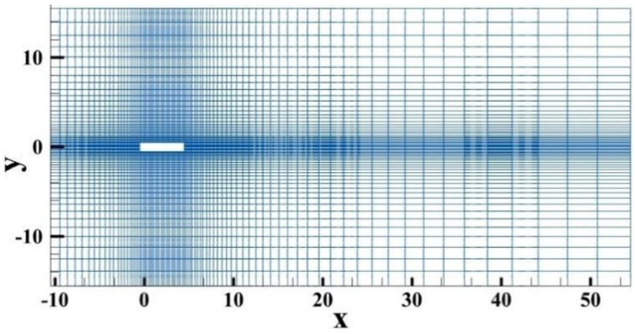

FIG. 1. Computational domain and mesh.

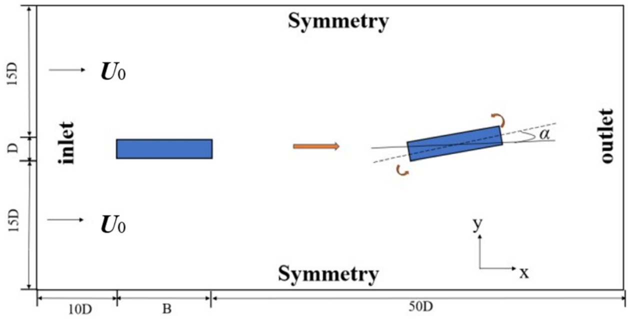

FIG. 2. Computational boundary conditions definition sketch.

the airflow, as shown in Fig. 2. The overall dimensionless quantities, including the lift coefficient (C_L), the drag coefficient (C_D), and the St number, are expressed as

$$C_l = \frac{F_l}{0.5\rho U_0^2 D}, \tag{3}$$

$$C_D = \frac{F_d}{0.5\rho U_0^2 D}, \tag{4}$$

$$St = \frac{fD}{U_0}, \tag{5}$$

where ρ is the fluid density and f is the fundamental frequency of vortex shedding in the flow.

B. Higher-order dynamic mode decomposition (HODMD)

HODMD can effectively extract the main dynamic modes along with corresponding frequencies and growth rates from the time series data. Following Koopman's assumption, a linear operator A and a residual matrix R are introduced to transform the "before" snapshot matrix U_{N-1} into the "after" snapshot matrix U:

$$AU_{N-1} = U_N + R, \tag{6}$$

$$U_{N-1} = [u_1,\ u_2,\ u_3,\ \ldots,\ u_{N-1}], \tag{7}$$

$$U_N = [u_2,\ u_3,\ u_4,\ \ldots,\ u_N]. \tag{8}$$

In contrast to DMD, which uses singular value decomposition to approximate the linear operator A, HODMD identifies low-dimensional subspaces by solving an optimization problem. Specifically, it finds the best mapping approximation by minimizing the residual matrix R. The minimization problem can be formulated as

$$\begin{gathered} \min \|\ U_N - AU_{N-1}\|^2 = \min \sum_{i=1}^{N} \|\ u_{i+1} - Au_i\ \|_2^2, \\ \text{such that } L^{\mathrm{T}}L = I, M \in R^{r\times r},\ L \in R^{p\times r}. \end{gathered} \tag{9}$$

We use the notation $\|\cdot\|_2$ to denote the Frobenius norm of a matrix, where r is the rank of the operator matrix $A = LML^T$, which is usually less than p. To estimate the initial dynamical system, we apply a low-rank decomposition $A = LML^T$. The rank-bounded expression for the equation can be derived as follows:

$$\begin{gathered} \min \|U_N - LML^{\mathrm{T}}U_{N-1}\|^{\ 2}, \\ \mathrm{M} \in R^{r\times r}, \quad L \in \left\{R^{p\times r} | L^{\mathrm{T}}L = I,\ k < p\right\}. \end{gathered} \tag{10}$$

Here, L denotes the low-dimensional subspace where each column of L is an orthonormal basis describing the shape of the intrinsic modes. The matrix M, on the other hand, serves as a projection operator providing a linear approximation of the system's evolution. The goal is to find the optimal matrices L and M that minimize the number of paradigms in Eq. (7). According to Wynn *et al.*,[37] this minimization problem can be tackled with flow optimization methods and reformulated as

$$\max_g(L) = \|L^{\mathrm{T}}U_N Q(L)^2\|,$$

Such that

$$\begin{gathered} L \in \left\{R^{p\times r} | L^{\mathrm{T}}L = I, k < p\right\}, \\ Cl(L) = U_{N-1}^{\mathrm{T}}\left(L^{\mathrm{T}}U_{N-1}L\right)^{-1}L^{\mathrm{T}}U_{N-1}. \end{gathered} \tag{11}$$

The least squares method can be used to determine the optimal low-order subspace basis L_i and its associated linear dynamics $M(L_i)$. The eigenvalues of the DMD can be expressed in logarithmic form as

$$\lambda_i = \frac{\log\mu_i}{\Delta t}. \tag{12}$$

Here λ_i represents the eigenvalue of matrix M. The real part of λ_i determines the temporal stability and reflects its growth rate, while the imaginary part determines the frequency of the mode. The dynamic mode ϕ_i associated with a specific λ_i is defined as:

$$\phi_i = Ly_i, \tag{13}$$

where *yi* denotes the eigenvector of matrix M. The projection parameter a_i, which signifies the modal amplitude, is defined as:

$$a_i = \left(\phi^{-1}\right)_{ij}(u_1)_j. \tag{14}$$

The energy of each mode E_i is determined by the product of the mode and its corresponding projection parameter

$$E_i = |a_i\phi_i|. \tag{15}$$

The *m*th primordial flow field can be expressed as

$$u_m = \sum_{i=1}^{n} a_i\varphi_i\lambda^{m-1}. \tag{16}$$

HODMD extends the initial observation matrix V_1^K int o matrix V_1^{K-d+1} with the required dimensions through d-order exponentially delayed snapshots. Here, V_1^{K-d+1} is a submatrix consisting of the first $K-\mathrm{d}$ columns and the last $K-\mathrm{d}$ columns of the modified snapshot matrix. Next, V_1^{K-d+1} is used as input data for the subsequent steps of the standard DMD.

$$V_1^{K-d+1} = \begin{bmatrix} V_1^{K-d+1} \\ V_2^{K-d+2} \\ \cdots \\ V_{d-1}^{K-1} \\ V_d^K \end{bmatrix}. \tag{17}$$

C. Floquet instability

To investigate the three-dimensional onset of flow around the rectangular cylinder, we used the same two-dimensional mesh and boundary conditions for the Floquet analysis. To derive the linearized N–S equations, we superimposed three-dimensional perturbations $u'(x, y, z, t)$ and $p'(x, y, z, t)$ onto the base flow field, resulting in the combined velocity $u(x, y, z, t)$ and pressure $p(x, y, z, t)$ as:

$$u(x, y, z, t) = U(x, y, t) + u'(x, y, z, t), \tag{18}$$

$$p(x, y, z, t) = P(x, y, t) + p'(x, y, z, t). \tag{19}$$

The linearized N–S equation is obtained by neglecting higher-order terms in the N–S equation

$$\nabla \cdot u' = 0. \tag{20}$$

After accounting for the pressure term implicitly, the evolution equation for the tiny perturbation can be simplified as follows:

$$\frac{\partial u'}{\partial t} = H(u'). \tag{21}$$

As the system is homogeneous in the z-direction, the general perturbations of the velocity and pressure fields can be expressed using a Fourier transform as:

$$u'(x, y, z, t) = \int_{-\infty}^{+\infty} \hat{u}(x, y, \beta, t) \mathrm{e}^{-i\beta z} \mathrm{d}\beta, \tag{22}$$

$$p'(x, y, z, t) = \int_{-\infty}^{+\infty} \hat{p}(x, y, \beta, t) \mathrm{e}^{-i\beta z} \mathrm{d}\beta. \tag{23}$$

Here, β represents the spanwise wave number, and the corresponding spanwise wavelength is $\lambda = 2\pi/\beta$. In the linearized N–S equations, the modes corresponding to different wave numbers are decoupled, and the system's overall response is obtained by superposing individual harmonics. The equations for a specific spanwise wavelength are as follows:

$$\frac{\partial \hat{u}}{\partial t} = H\big(U, \beta, \hat{u}(x, y, t)\big). \tag{24}$$

The process is numerically implemented as follows: The 2D flow field data are collected at 32 equally spaced intervals within a single vortex shedding cycle. The velocity field is then Fourier transformed over time to produce 32 complex Fourier coefficients. These coefficients are used in Floquet instability analysis to reconstruct the 2D base flow at any point within the shedding cycle. To solve for eigenvalues and eigenvectors during instability analysis, the Arnoldi algorithm in a Krylov subspace of dimension $Kn = 32$ is used.[38]

D. Verification

This section examines the effects of mesh resolution and polynomial order N_P on the simulation results and accuracy. Table I presents numerical simulation results for four mesh resolutions and the accuracy of this study is evaluated by comparing and analyzing the St and C_D of rectangular cylinders at $\alpha = 0°$ and $Re = 200$. These results are also compared with findings from other studies. The maximum difference among different mesh resolutions is no more than 1%. Considering both accuracy and computational efficiency, a grid resolution of 5548 with $N_P = 6$ is utilized in this study.

TABLE I. Comparison of simulation results for four N_P and with earlier literature.

	N_P	Re	St	C_D
Present stationary Case ($\alpha = 0°$)	4	200	0.1428	1.0336
	5		0.1441	1.04
	6		0.1433	1.0376
	7		0.1433	1.0396
Zhu *et al.*[6]	⋯	200	0.1412	1.028
Patruno *et al.*[39]	⋯	2.7 × 104	0.132	1.02

III. RESULTS AND DISCUSSION

A. Fluid force coefficients

Figures 3(a) and 3(b) show the variation of the mean drag coefficient ($\bar{C}_D$) and the root mean square of the lift coefficient (C'_L) with increasing angle of attack for rectangular cylinders with an aspect ratio (AR) of 5 at Re of 200, 250, and 300, respectively. From Fig. 3(a), the trends of $\bar{C}_D$ are essentially the same across different Re, and $\bar{C}_D$ increases approximately linearly with minor differences as α increases. As α increases, a progressively larger cavity forms beneath the rectangular cylinder, affecting the position of the flow separation point, vortex shedding frequency, and pressure distribution around the rectangular cylinder. This, in turn, influences the drag and lift forces on the rectangular cylinder. The drag force is expected to increase with α, and the flow separation region will expand. Consequently, $\bar{C}_D$ will continue to increase.

In Fig. 3(b), for $\alpha < 6°$, C'_L increases approximately linearly. For $Re = 250$ and 300, the gradient of C'_L starts to decrease for $\alpha > 8°$, and the change tends to flatten out. This indicates that lift fluctuation increases significantly with α at low α, and the rate of increase in lift fluctuation begins to slow down beyond $\alpha = 8°$. However, for $Re = 200$, C'_L continues to increase rapidly in this α range. The values of C'_L differ significantly across Re, while the values of $\bar{C}_D$ show little variation. This indicates that Re has a greater impact on the lift coefficient than the drag coefficient. Higher Re corresponds to larger amplitudes of lift fluctuation.

The St number denotes the dimensionless frequency of vortex shedding, determined by the fundamental frequency in the power spectral density (PSD). Variation in the St number reflects tail flow separation and changes in the vortex shedding mode. Figure 4(a) shows the variation of St with α at three different Re. The figure shows that the St number generally decreases with increasing α, indicating decreased vortex shedding frequency. However, the decrease in St is not continuous, with a slight increase observed in the α range of 2°–6° for $Re = 250$ and 300, possibly due to changes in the vortex shedding mode. Additionally, we observed that the lift time-duration curves at intermediate α associated with the 3D transition of the wake (2.5° for $Re = 200$, 1.5° for $Re = 250$, and 0.5° for $Re = 300$) do

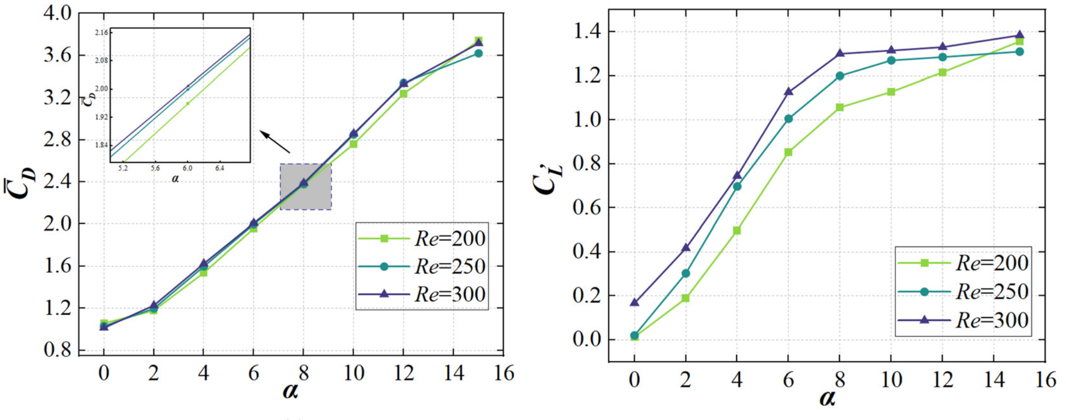

(a) (b)

FIG. 3. (a) Variation of $\bar{C}_D$ with α at different *Re*; (b) variation of *C′L* with α at different *Re*.

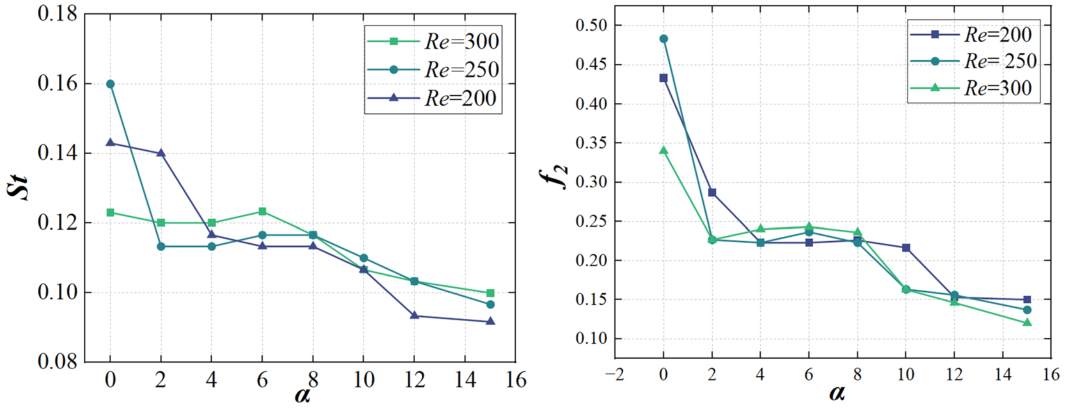

(a) (b)

FIG. 4. (a) Variation of *St* number with α at different *Re*; (b) variation of the secondary frequency f_2 with α at different *Re*.

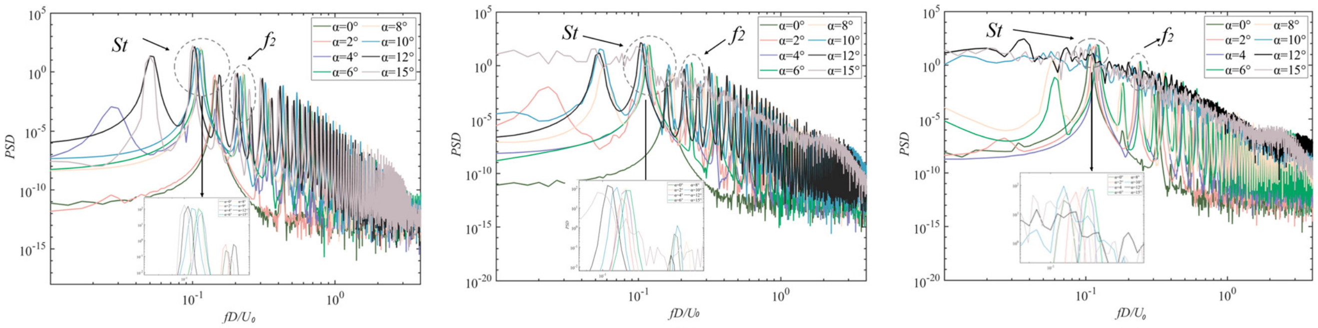

(a) (b) (c)

FIG. 5. Power spectral density (PSD): (a) *Re* = 200, (b) *Re* = 250, and (c) *Re* = 300.

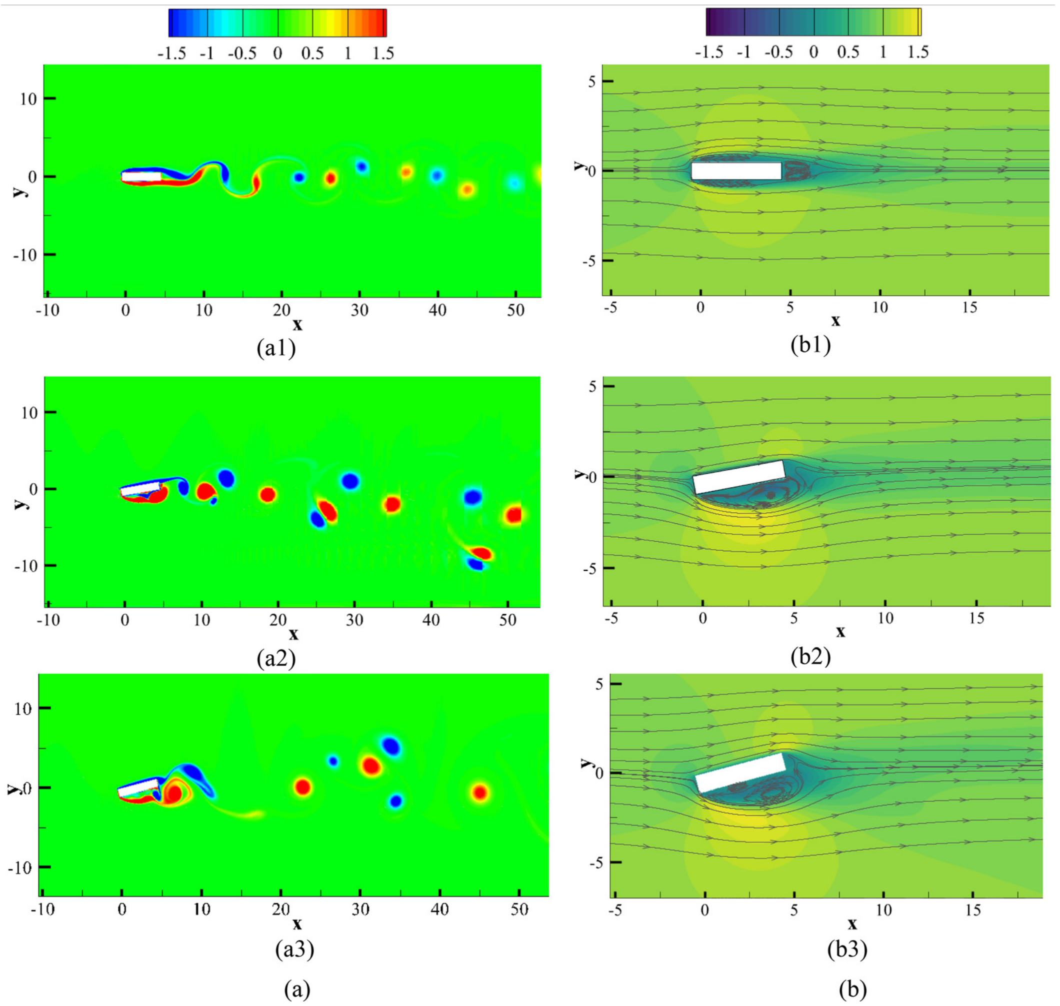

FIG. 6. (a) Instantaneous base flow structures at $Re = 300$: (a1) $\alpha = 0°$, (a2) $\alpha = 10°$, and (a3) $\alpha = 15°$. (b) Mean flow velocity in the x-direction at $Re = 300$: (b1) $\alpha = 0°$, (b2) $\alpha = 10°$, and (b3) $\alpha = 15°$.

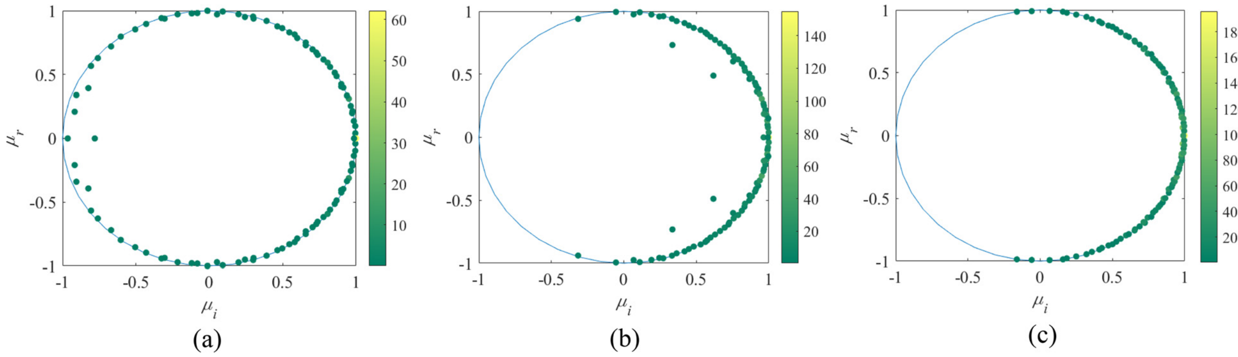

FIG. 7. Ritz values vs unit circle: (a) $\alpha = 0°$ and $Re = 300$ (b) $\alpha = 10°$ and $Re = 300$, and (c) $\alpha = 15°$, and $Re = 300$.

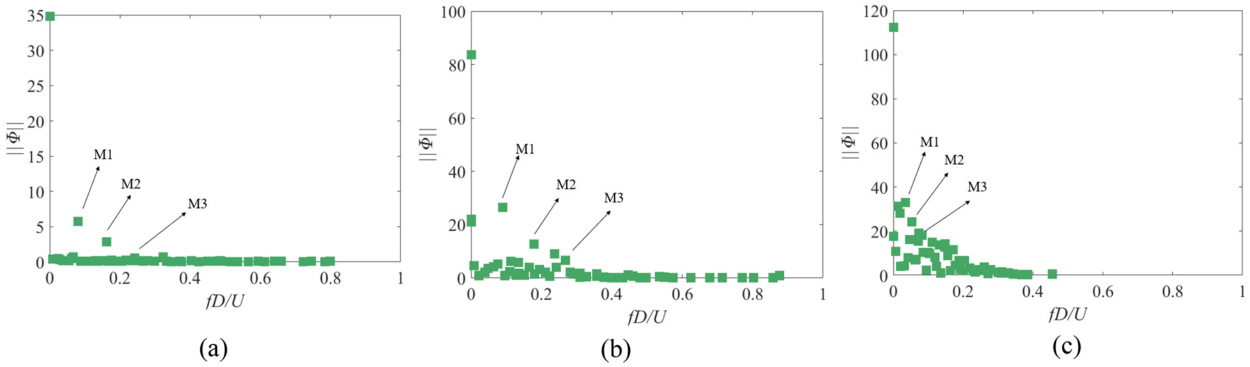

FIG. 8. Mode energy as a function of frequency: (a) $\alpha = 0°$ and $Re = 300$ (b) $\alpha = 10°$ and $Re = 300$, and (c) $\alpha = 15°$ and $Re = 300$.

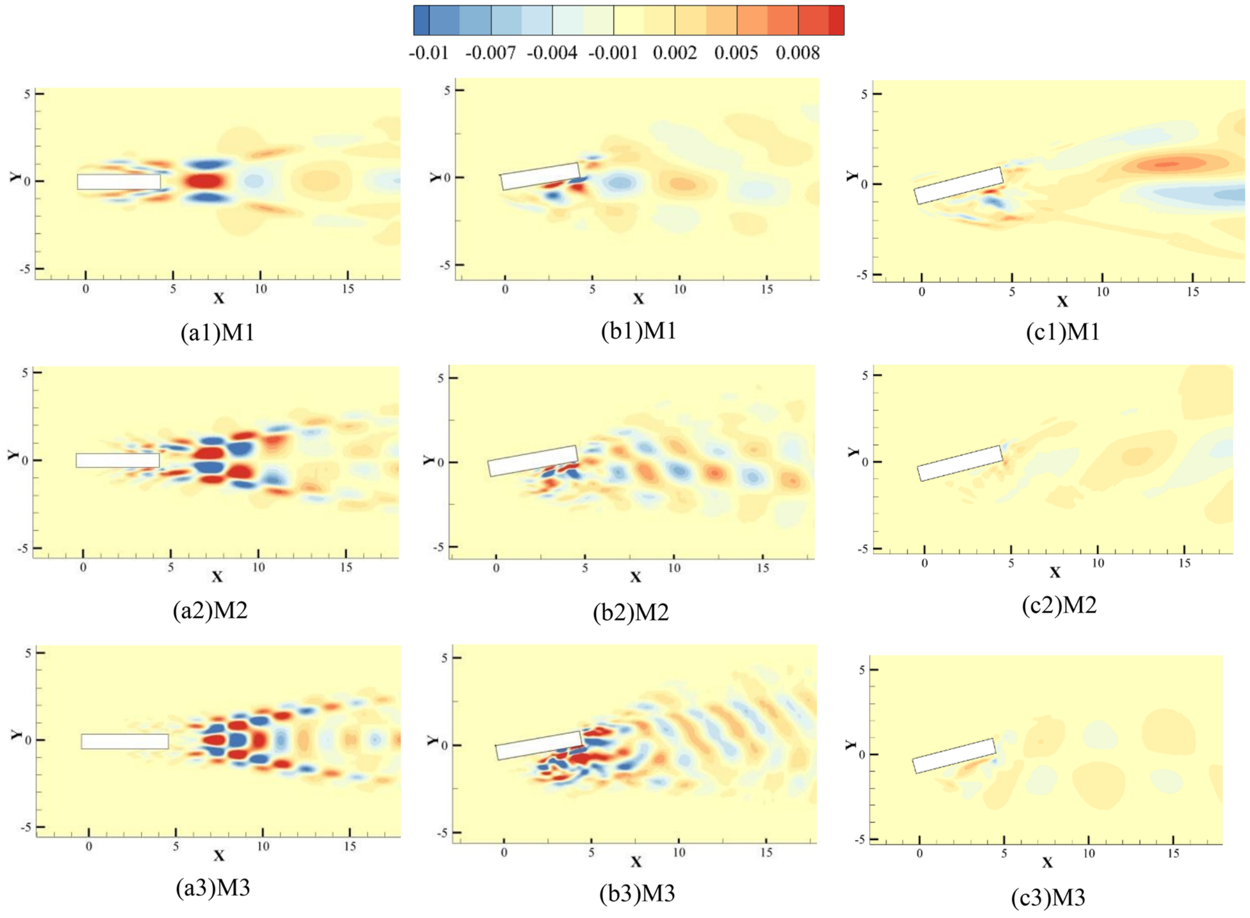

FIG. 9. First three orders of vorticity modes at $Re = 300$. Mode (a1), (a2), and (a3) at $\alpha = 0°$; (b) mode (b1), (b2), and (b3) at $\alpha = 10°$; and (c) mode (c1), (c2), and (c3) at $\alpha = 15°$.

not exhibit the typical simple harmonic waveform seen at other α but instead display an irregular waveform. The figure shows that the overall trend of the *St* number is similar across different *Re*. The second harmonic of the power spectral density of the flow corresponds to the sub-frequency, indicating the secondary instability of the flow. The second harmonic is shown in Fig. 4(b), and the PSD curves for the three *Re* are shown in Figs. 5(a)–5(c).

B. Higher-order dynamic modal decomposition analysis of the flow field

The 2D instantaneous base flow structures and mean flow velocity fields for $\alpha = 0°$, $10°$, and $15°$ at $Re = 300$, obtained through numerical simulations, are shown in Figs. 6(a) and 6(b). These figures reveal the transient features of the flow and the time-averaged distribution. However, subtle structures and potential changes in the flow are difficult to discern. Therefore, we applied the HODMD method to these flow fields for deeper analysis.

HODMD is suitable for analyzing systems with complex nonlinear behavior, especially for examining periodic flow phenomena such as vortex shedding. HODMD extracts dominant modes and flow structures, allowing for a downscaled representation of the flow field, and facilitating a deeper investigation of the main features and modes of the flow. This section synchronously decomposes the vorticity and pressure field to extract the global modal energy ($|ai|$) and local modal shapes ($|\varphi i|$) used to characterize the flow. In each case, fifteen oscillatory cycles were sampled, with each cycle containing 20 samples, corresponding to an interval period of $T/20$ The data were collected after the flow conditions were fully developed. As shown in Figs. 7(a)–7(c), the Ritz values λ_i of the dominant modes all lie within the expected unit circle. Points on the unit circle indicate that the corresponding fluid modes are in a limit-cycle oscillatory state, suggesting that the dynamical behavior of the system is stable and that this method effectively captures the eigenfrequencies of the system's dynamics.

The first three data points are labeled M1, M2, and M3, with dimensionless frequencies: M1: $fD/U_0 = St$, M2: $fD/U_0 = 2\,St$, and M3: $fD/U_0 = 3\,St$, which correspond to the first three dynamic modes shed by the wake vortex, respectively. As shown in Figs. 8(a)–8(c), the energy levels of M2 and M3 are significantly lower than that of M1, indicating that the wake is co-dominated by these three modes, with the main mode (M1) exerting a much greater influence on the wake than the other two super harmonic modes (M2 and M3) The increase in the angle of attack leads to a significant rise in the energy of the first three modes, implying that the strength and energy of vortex shedding continuously increase, resulting in an increased loading effect on the surface of the rectangular cylinder.

C. Vorticity and pressure modal analysis

Figures 9 and 10 display the first three orders of vorticity and pressure modes for angles of attack 0°, 10°, and 15°. The lower-order modes depict larger-scale, low-frequency vortex

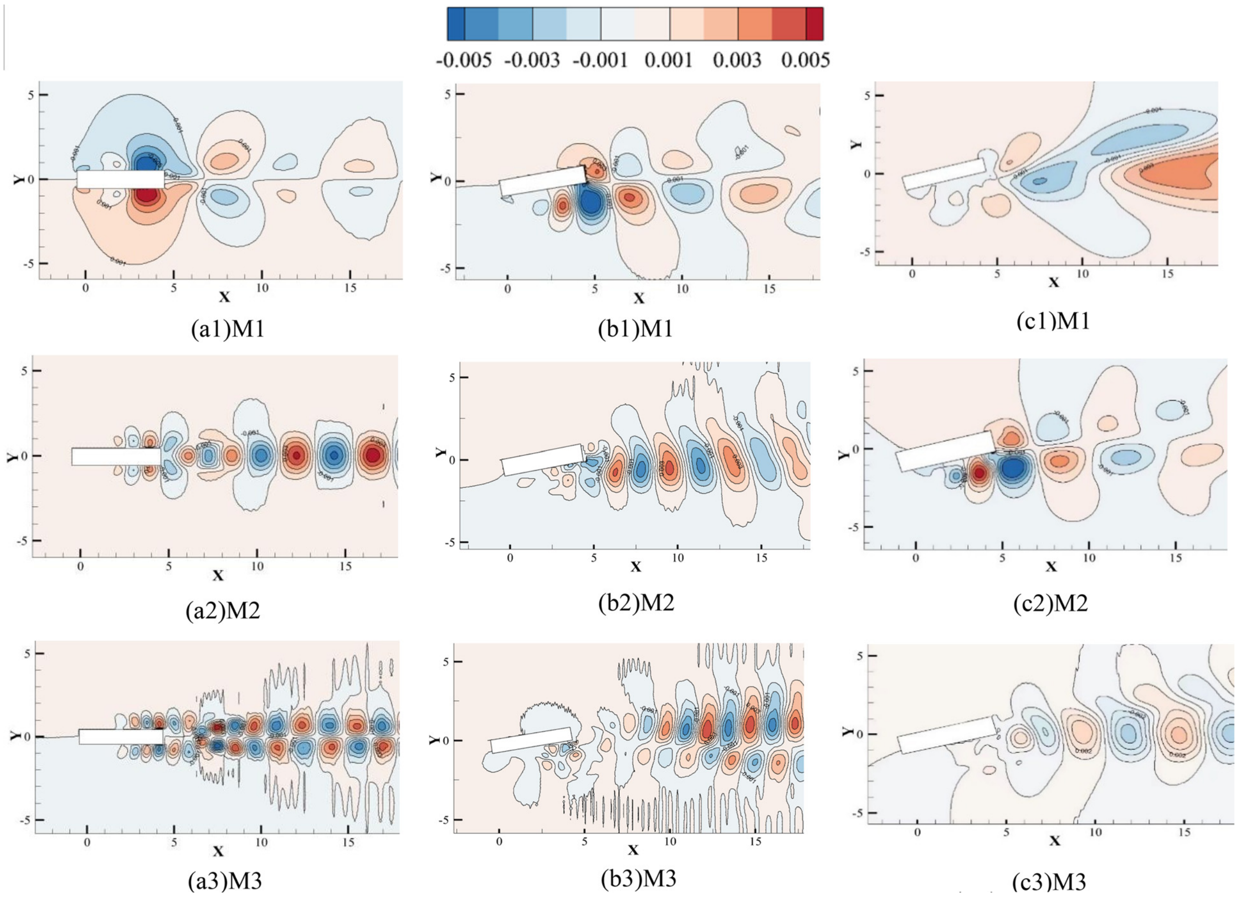

(a1)M1 (b1)M1 (c1)M1

(a2)M2 (b2)M2 (c2)M2

(a3)M3 (b3)M3 (c3)M3

FIG. 10. First three orders of pressure modes at $Re = 300$. (a) Mode (a1), (a2), and (a3) at $\alpha = 0°$; (b) mode (b1), (b2), and (b3) at $\alpha = 10°$; and (c) mode (c1), (c2), and (c3) at $\alpha = 15°$.

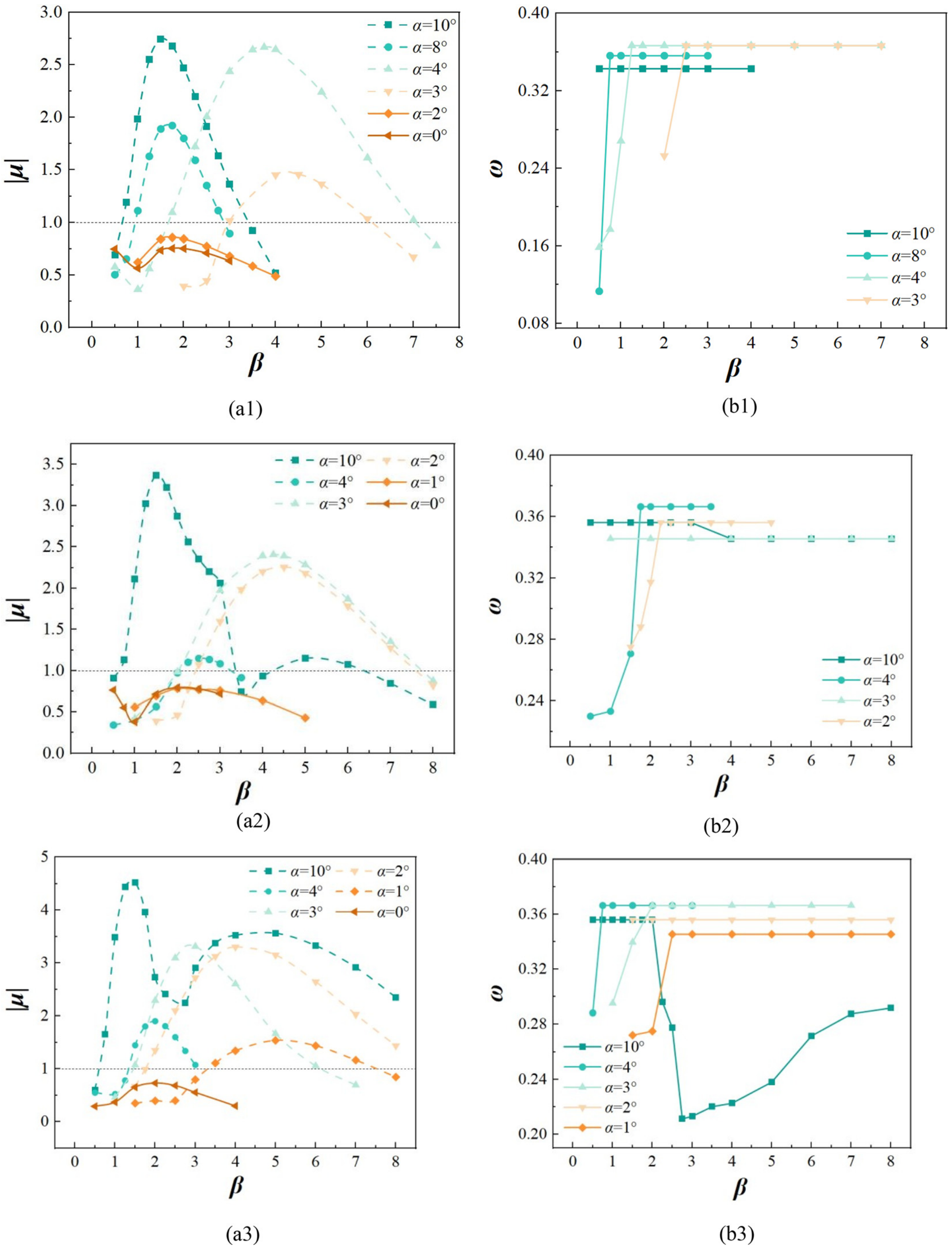

(a1) (b1)

(a2) (b2)

(a3) (b3)

FIG. 11. (a) Variation of the Floquet multiplier ($|\mu|$) with the spanwise perturbation wave number (β) at different α: (a1) $Re = 200$, (a2) $Re = 250$, and (a3) $Re = 300$. (b) Variation of frequency (ω) with the spanwise perturbation wave number (β) at different α: (b1) $Re = 200$, (b2) $Re = 250$, (b3) $Re = 300 = 250$, and (c) $=300$.

motions that are detached from the flow and generally contain most of the flow's energy. In contrast, higher-order modes correspond to smaller-scale, higher-frequency vortex structures and turbulence that are more complex. Different colors in the figures represent vorticity and pressure in opposite directions, respectively.

When $\alpha = 0°$, the vorticity and pressure of the low-order modes are mainly concentrated near the trailing edge of the model. Vorticity and pressure intensify at the far trailing edge as the mode order increases, indicating that large-scale flow separation mainly occurs near the trailing edge, while complex turbulence primarily occurs at the far trailing edge. Odd-order vorticity modes are symmetrically distributed, while even-order modes are antisymmetric; the pressure modes exhibit the opposite distribution. The distribution pattern of pressure modes is opposite, with odd-order modes distributed antisymmetrically and even-order modes symmetrically. The moments generated by vortices in different directions cancel each other, indicating that odd-order modes have a larger effect on the lift force, while even-order modes have a weaker effect.

At $\alpha = 10^\circ$, the first three vorticity modes are concentrated around the trailing edge and lower cavity of the rectangular model. This concentration indicates the presence of more vortical structures of varying scales and frequencies in these regions, along with enhanced flow separation. The alternating left-right pattern of the vorticity distribution weakens, suggesting a transition from periodic to aperiodic flow structures, with vortices becoming increasingly irregular. Additionally, the rearward shift in the distribution of the first three pressure modes indicates that larger-scale vortices form at the leading edge and midsection of the model, dominating the initial flow separation and reattachment processes. As the flow moves downstream, smaller-scale vortices gradually dominate in the trailing edge and separation regions.

When $\alpha = 15^\circ$, the vorticity modal map lacks symmetry and alternating patterns, indicating a non-periodic flow structure. Increasing the angle of attack results in a more complex flow structure and enhanced nonlinearity. A large range of modal distributions is observed from the first-order vorticity and pressure modes, indicating that the influence of flow separation is widespread. The vorticity modes exhibit significant irregularity, while the odd-order pressure modes show high concentration in the downstream region, suggesting that the flow structure at the far edge is undergoing a large-scale transition to a turbulent state.

D. Floquet instability analysis

Floquet analysis is commonly used to predict the stability of periodic flows. In this section, we utilized Floquet analysis to determine the linear stability of a periodic base flow to 3D perturbations and to evaluate the system's response to these perturbations. This method has been widely used in various models and shapes for periodic stability analysis.[40–42] The modulus of the Floquet multiplier is denoted by $|\mu|$. If $|\mu|$ is less than 1, the base flow is stable, and 3D perturbations will diminish, returning the flow to its initial state. When $|\mu| > 1$, the base flow is unstable, and perturbations will grow exponentially, leading to a 3D wake structure. The Floquet multiplier is a complex number. If the Floquet multiplier has only a positive or negative real part, the Floquet mode will be Modes A, B, or C, with periods equal to or multiples of the base flow period. If the Floquet multiplier contains non-zero imaginary components, the Floquet mode will be a quasi-periodic mode with periods that are not proportional to the base flow period (Mode QP). As illustrated in Fig. 11(a), the solid line represents Mode A, the dashed line represents Mode QP, and the horizontal black dotted line indicates the neutral instability threshold. Frequency, a critical parameter, is depicted in Fig. 11(b). The primary objective of this section is to determine the transition angle of attack α_{3D} at which the flow starts to exhibit strong 3D characteristics, while the secondary objective is to investigate the unsteady modes of the wake post the application of perturbations. Based on the HODMD analysis from the previous section, it is observed that the flow structure begins to display non-periodic behavior as α increases to 10°. Therefore, this section will solely examine cases where α is less than or equal to 10°.

At $Re = 200$, as shown in Fig. 11(a1), α_{3D} range between 2° and 3°. When α is less than 2°, the flow remains stable against infinitesimal 3D perturbations. However, if α exceeds 3°, the 3D perturbations will amplify over time, ultimately imparting strong 3D characteristics to the flow field. As Re increases, α_{3D} shows a decreasing trend, which is consistent with the findings of Siddharth Gupta *et al.* in their study of wing modeling. As shown in Figs. 11(a2) and 11(a3), for $Re = 250$ and 300, the transition α_{3D} decreases to between 1° and 2° and between 0° and 1°, respectively. Overall, the Floquet multiplier value increases as α increases, indicating a corresponding increase in flow instability. Interestingly, after exceeding the transition angle of attack α_{3D}, the first Floquet instability Mode QP appears at larger spanwise wave numbers and with a broader range of spanwise wave numbers. As α continues to increase toward a certain value, Mode QP rapidly shifts to lower spanwise wave numbers, and the range of spanwise wave numbers quickly narrows. Although the gradient of the Floquet multiplier's growth increases, the overall value of the Floquet multiplier decreases compared to before. This suggests that instability grows faster for smaller spanwise wave numbers than larger ones.

We refer to the spanwise wave number at which the growth rate of the Floquet modes reaches its maximum and the Floquet multiplier attains its highest value as the dominant wave number. At this wave number, the linear instability of the flow is strongest, perturbations grow at the fastest rate, and the wake system is most likely to destabilize. The most unstable case of the system occurs at $\alpha = 10^\circ$and $\beta = 1.5$. Comparing $Re = 200$, 250, and 300, the variations in dominant wave numbers between long and short waves, as well as between short and short waves, are less affected by the Reynolds number. This aligns with the findings of Naghib-Lahouti *et al.*,[43] who studied a typical blunt body with an elliptical front edge and a rectangular rear edge at moderate Re. The dominant wave number shifts significantly along the x-axis as α increases,

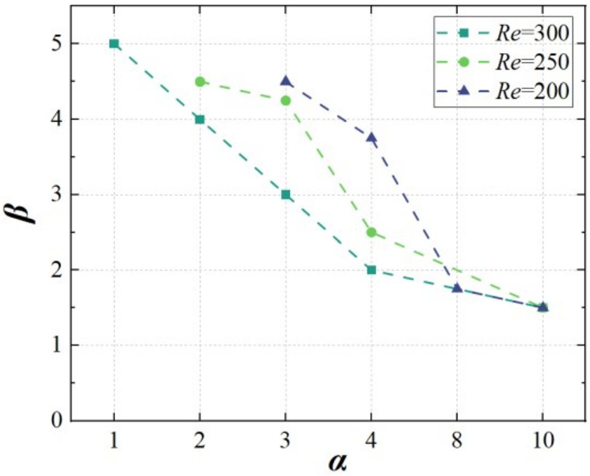

FIG. 12. Variation of dominant wave number (β) with α at different *Re*.

with this shift being more pronounced for $Re = 300$. For comparison, Fig. 12 presents the variation of the dominant wave number to α. Additionally, at $Re = 250$ and 300 with $\alpha = 10°$, we observe two unstable bands: one for short waves ($3.5 < \beta < 8$) and one for long waves ($1 < \beta < 3$). The system is more prone to destabilization with the short-wave unstable bands compared to the long-wave bands.

E. Floquet modal properties

This section presents the properties of each Floquet mode by analyzing the streamwise vorticity field of the wake and comparing the differences between the various modes. Figure 13(a1) shows the streamwise vorticity field at $\alpha = 2°$ and $Re = 200$, while Fig. 13(b1) presents the 3D view of the Floquet mode in this case. The Floquet mode observed here is Mode A, with all Floquet multipliers being real. This mode can persist far downstream, and it shares similarities with Mode A of the cylinder in that it exhibits spatiotemporal odd symmetry—symmetric in space along the y-axis, with a half-period shift in time (i.e., $t + T/2$) and a sign reversal.

$$\widetilde{\omega}_x(x, y, z, t) \simeq -\widetilde{\omega}_x\left(x, -y, z, t + \frac{T}{2}\right). \tag{25}$$

The main difference from the cylindrical Mode A is that the streamwise vorticity of this Mode A is more concentrated in the braided shear layer rather than in the spanwise vortex core.

Figure 13(a2) shows the streamwise vorticity field at $\alpha = 4°$ and $Re = 250$, where the emergent Floquet mode is the quasi-periodic Mode (QP). This mode has subharmonic characteristics, with all Floquet multipliers being complex numbers with imaginary parts. Mode QP has similar spatial properties to Mode C, but unlike Mode C, it does not have a period exactly twice that of the base flow. As shown in the figure, Mode QP rotates in alternating clockwise and counterclockwise directions. Compared to Mode A, the quasi-periodic Mode QP exhibits more complex temporal and spatial evolution. Additionally, Mode QP becomes increasingly complex and irregular

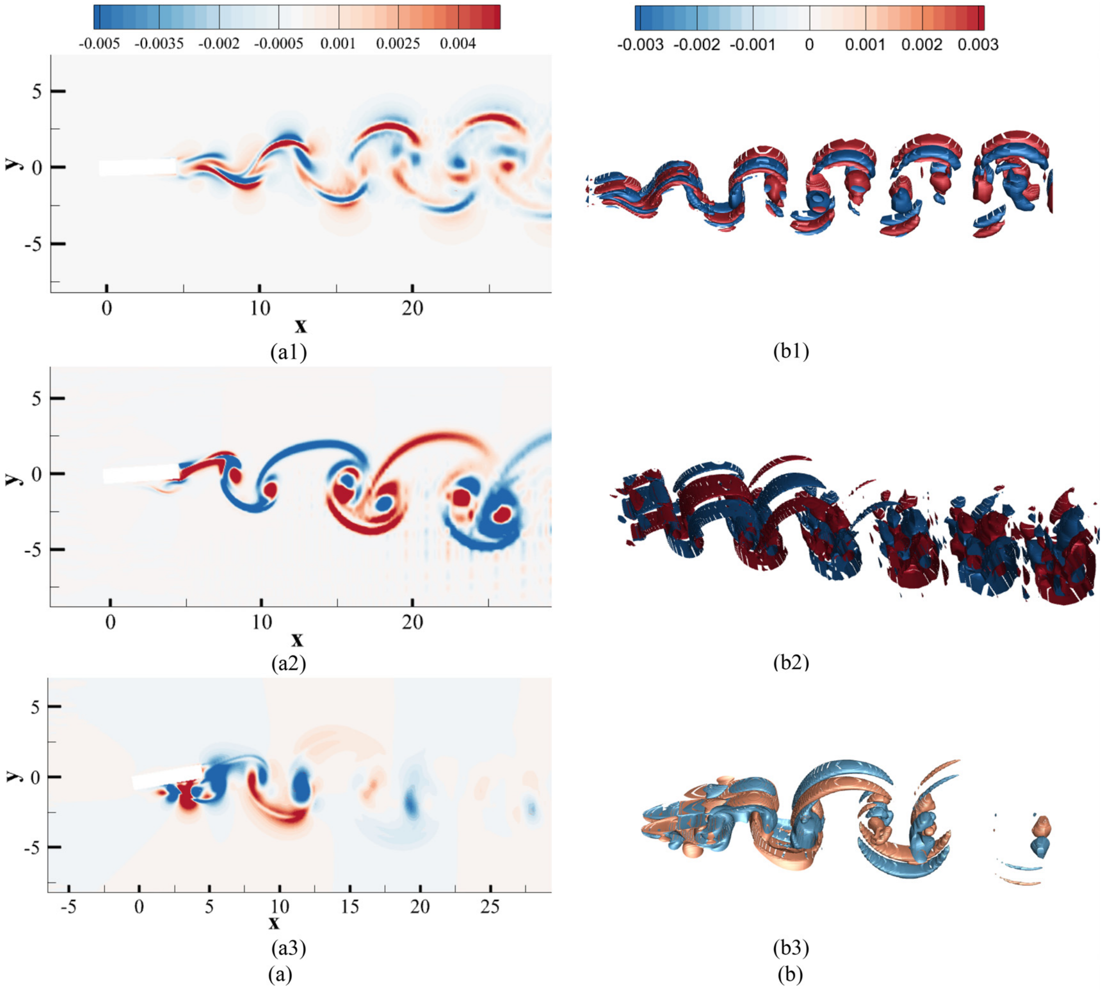

FIG. 13. (a) Floquet modal 2D plots: (a1) $\alpha = 2°$ and $Re = 200$, (a2) $\alpha = 4°$ and $Re = 250$, and (a3) $\alpha = 10°$ and $Re = 200$. (b) Floquet modal 3D plots: (b1) $\alpha = 2°$ and $Re = 200$, (b2) $\alpha = 4°$ and $Re = 250$, and (b3) $\alpha = 10°$ and $Re = 200$.

downstream, indicating that the flow structure is gradually destabilizing in that region. Figure 13(a3) shows the streamwise vorticity field at $\alpha = 10^\circ$ and $Re = 200$, where the Floquet modes are still quasi-periodic. However, compared to the typical quasi-periodic modes observed earlier, these modes dissipate rapidly in the wake and start to lose their order early in the flow. The HODMD analysis in the previous section indicates that this phenomenon may be attributed to the large number of spanwise vortices present in the lower cavity and trailing edge of the rectangular cylinder at medium and high α within the studied range. These vortices rapidly transition to turbulence downstream, subsequently affecting the attached streamwise vortices. Generally, the dynamic behaviors of the vortices differ at various angles of attack, which accounts for the significant differences in Floquet modes.

IV. CONCLUSION

This paper analyzes the flow characteristics of a rectangular cylinder with an aspect ratio of 5 under varying α and *Re*. Through in-depth exploration using HODMD and Floquet analysis, the following conclusions are drawn:

1. In the studied range of α, both the mean drag coefficient ($\bar{C}_D$) and the root mean square of the lift coefficient (C'_L) increase with α. The increase in$\bar{C}_D$is stable and continuous, while C'_L increases more slowly after $\alpha = 8^\circ$. Additionally, *Re* has a more pronounced effect on C'_L than on$\bar{C}_D$.The increase in α results in a discontinuous decrease in the *St* number.
2. An increase in α will lead to an increase in the modal energy of vortex shedding. When $\alpha = 0^\circ$, odd-order modes are the primary contributors to lift, with low-order modes concentrated near the trailing edge and high-order modes at the far trailing edge. When $\alpha = 10^\circ$, the modal distribution is no longer completely symmetric, and the alternating pattern weakens, with modes mainly concentrated at the trailing edge of the rectangular cylinder and the lower cavity. When $\alpha = 15^\circ$, the vorticity modes exhibit significant irregularity, while the odd-order pressure modes show high concentration in the downstream region, and the range of first-order vorticity and pressure modes is relatively large.
3. The 3D transition angles of attack for $Re = 200$, 250, and 300 are 2°–3°, 1°–2°, and 0°–1°, respectively. As α increases, there is a sudden change in the unstable bands of the flow structure to the perturbation wave numbers. When $\alpha = 10^\circ$, two unstable bands are observed for $Re = 250$ and $Re = 300$. The variations in the dominant wave numbers between long waves and short waves are less influenced by *Re* and more affected by α.
4. Within the scope of this study, two types of Floquet modes are identified: Mode A and the quasi-periodic Mode QP. The streamwise vorticity of Mode A is more prominently found in the braided shear layer. This mode can persist far downstream. The quasi-periodic Mode QP becomes complex and irregular at the far trailing edge, with the mode at $\alpha = 10^\circ$ and $Re = 200$ dissipating rapidly in the wake.

This study offers valuable insights into the flow evolution mechanisms of rectangular cylinders at various α and *Re*. It is particularly significant for understanding flow structures and 3D instabilities, providing important references for engineering applications. This also provides a valuable reference for engineering applications or fields that require control of flow loads in the spanwise direction.

ACKNOWLEDGMENTS

The authors would like to thank the support of the Hainan Provincial Natural Science Foundation of China (Grant No. 524QN224), the Open Research Project of Key Laboratory for Intelligent Infrastructure and Monitoring of Fujian Province (Grant No. IIM-01-02), and the Natural Science Foundation of Heilongjiang Province China (Grant No. LH 2020E010). The numerical calculations in this paper have been done at Hefei's advanced computing center.

AUTHOR DECLARATIONS

Conflict of Interest

The authors have no conflicts to disclose.

Author Contributions

Lingyu Qiao: Conceptualization (equal); Data curation (equal); Methodology (equal); Software (equal); Visualization (equal); Writing – original draft (equal). **Ying Zhao:** Conceptualization (equal); Formal analysis (equal); Supervision (equal); Validation (equal); Writing – review & editing (equal). **Lei Zhou:** Conceptualization (equal); Formal analysis (equal); Methodology (equal). **Yifeng Ai:** Conceptualization (equal); Formal analysis (equal). **Qingchi Zhu:** Conceptualization (equal); Methodology (equal). **Hongfu Zhang:** Conceptualization (equal); Formal analysis (equal); Funding acquisition (equal); Validation (equal); Writing – review & editing (equal).

DATA AVAILABILITY

The data that support the findings of this study are available from the corresponding authors upon reasonable request.

REFERENCES

[1] F. Ricciardelli and A. M. Marra, presented at the Proceedings of the 6th International Colloquium on Bluff Body Aerodynamics and Applications, Milan, Italy, 2008.

[2] Y. Nakamura and M. Nakashima, "Vortex excitation of prisms with elongated rectangular, H and [vdash] cross-sections," J. Fluid Mech. **163**, 149–169 (1986).

[3] Y. Nakamura, Y. Ohya, and H. Tsuruta, "Experiments on vortex shedding from flat plates with square leading and trailing edges," J. Fluid Mech. **222**, 437–447 (1991).

[4] L. Bruno, M. V. Salvetti, and F. Ricciardelli, "Benchmark on the aerodynamics of a rectangular 5: 1 cylinder: An overview after the first four years of activity," J. Wind Eng. Ind Aerodyn. **126**, 87–106 (2014).

[5] L. Bruno, D. Fransos, N. Coste, and A. Bosco, "3D flow around a rectangular cylinder: A computational study," J. Wind Eng. Ind Aerodyn. **98**(6–7), 263–276 (2010).

[6] L. Zhou, Q. Zhu, K. Tse, X. Ning, Y. Ai, and H. Zhang, "Flow pattern-and forces-susceptibility to small attack angles for a rectangular cylinder," Ocean Eng. **300**, 117376 (2024).

[7] Q. Zhu, L. Zhou, K. T. Tse, X. Ning, and H. Zhang, "Aerodynamic interference effects of bridge-train-like bluff bodies with small flow attack angle," Phys. Fluids **36**(9), 093621 (2024).

[8] G. Schewe, "Reynolds-number-effects in flow around a rectangular cylinder with aspect ratio 1: 5," J. Fluids Struct. **39**, 15–26 (2013).

[9] K. Shimada and T. Ishihara, "Predictability of unsteady two-dimensional k$-\varepsilon$ model on the aerodynamic instabilities of some rectangular prisms," J. Fluids Struct. **28**, 20–39 (2012).

[10] D. T. Nguyen, D. M. Hargreaves, and J. S. Owen, "Vortex-induced vibration of a 5: 1 rectangular cylinder: A comparison of wind tunnel sectional model tests and computational simulations," J. Wind Eng. Ind Aerodyn. **175**, 1–16 (2018).

[11] P. J. Schmid, "Dynamic mode decomposition of numerical and experimental data," J. Fluid Mech. **656**, 5–28 (2010).

[12] A. T. Mohan, D. V. Gaitonde, and M. R. Visbal, "Model reduction and analysis of deep dynamic stall on a plunging airfoil," Comput. Fluids **129**, 1–19 (2016).

[13] H. Zhang, L. Zhou, T. Liu, Z. Guo, and F. Golnary, "Dynamic mode decomposition analysis of the two-dimensional flow past two transversely in-phase oscillating cylinders in a tandem arrangement," Phys. Fluids **34**(3), 033602 (2022).

[14] S. Le Clainche and J. M. Vega, "Higher order dynamic mode decomposition," SIAM J. Appl. Dyn. Syst. **16**(2), 882–925 (2017).

[15] Q. Zhu, H. Li, H. Zhu, L. Zhou, K. T. Tse, and H. Zhang, "Koopman mode analysis on discovering distributed energy transfer of post-transient flutter of a bluff body," Ocean Eng. **309**, 118557 (2024).

[16] N. Benito, J. Arias, A. Velazquez, and J. Vega, "Real time performance improvement of engineering control units via higher order singular value decomposition: Application to a SI engine," Control Eng. Pract. **19**(11), 1315–1327 (2011).

[17] Q. Zhu, L. Zhou, H. Zhang, K. T. Tse, H. Tang, and B. R. Noack, "A zero-net-mass-flux wake stabilization method for blunt bodies via global linear instability," Phys. Fluids **36**(4), 043617 (2024).

[18] T. Leweke and C. H. Williamson, "Cooperative elliptic instability of a vortex pair," J. Fluid Mech. **360**, 85–119 (1998).

[19] B. R. Noack and H. Eckelmann, "A global stability analysis of the steady and periodic cylinder wake," J. Fluid Mech. **270**, 297–330 (1994).

[20] D. Barkley and R. D. Henderson, "Three-dimensional Floquet stability analysis of the wake of a circular cylinder," J. Fluid Mech. **322**, 215–241 (1996).

[21] S. Leblanc and C. Cambon, "Effects of the Coriolis force on the stability of Stuart vortices," J. Fluid Mech. **356**, 353–379 (1998).

[22] L. Lin, S. Shi, and Y. Wu, "Intrinsic relationship of vorticity between modes A and B in the wake of a bluff body," Theor. Appl. Mech. Lett. **8**(5), 320–325 (2018).

[23] G. J. Sheard, M. C. Thompson, and K. Hourigan, "From spheres to circular cylinders: The stability and flow structures of bluff ring wakes," J. Fluid Mech. **492**, 147–180 (2003).

[24] G. J. Sheard, M. J. Fitzgerald, and K. Ryan, "Cylinders with square cross-section: Wake instabilities with incidence angle variation," J. Fluid Mech. **630**, 43–69 (2009).

[25] H. M. Blackburn, F. Marques, and J. M. Lopez, "Symmetry breaking of two-dimensional time-periodic wakes," J. Fluid Mech. **522**, 395–411 (2005).

[26] S. Gupta, J. Zhao, A. Sharma, A. Agrawal, K. Hourigan, and M. C. Thompson, "Two-and three-dimensional wake transitions of a NACA0012 airfoil," J. Fluid Mech. **954**, A26 (2023).

[27] A. Rao, J. Leontini, M. C. Thompson, and K. Hourigan, "Three-dimensionality in the wake of a rotating cylinder in a uniform flow," J. Fluid Mech. **717**, 1–29 (2013).

[28] D. Park and K.-S. Yang, "Effects of planar shear on the three-dimensional instability in flow past a circular cylinder," Phys. Fluids **30**(3), 034103 (2018).

[29] K. Ryan, M. C. Thompson, and K. Hourigan, "Three dimensional transition in the wake of bluff elongated cylinders," J. Fluid Mech. **538**, 1–29 (2005).

[30] S. Julien, S. Ortiz, and J.-M. Chomaz, "Secondary instability mechanisms in the wake of a flat plate," Eur. J. Mech. B **23**(1), 157–165 (2004).

[31] D. Yang, B. Pettersen, H. I. Andersson, and V. D. Narasimhamurthy, "Floquet stability analysis of the wake of an inclined flat plate," Phys. Fluids **25**(9), 094103 (2013).

[32] G. J. Sheard, "Wake stability features behind a square cylinder: Focus on small incidence angles," J. Fluids Struct. **27**(5–6), 734–742 (2011).

[33] C.-B. Choi, Y.-J. Jang, and K.-S. Yang, "Secondary instability in the near-wake past two tandem square cylinders," Phys. Fluids **24**(2), 024102 (2012).

[34] R. d S. Gioria, P. J. S. Jabardo, B. S. Carmo, and J. R. Meneghini, "Floquet stability analysis of the flow around an oscillating cylinder," J. Fluids Struct. **25**(4), 676–686 (2009).

[35] H. Zhang, D. Xin, J. Zhan, and L. Zhou, "Flow past a transversely oscillating cylinder at lock-on region and three-dimensional Floquet stability analysis of its wake," Phys. Fluids **33**(2), 025111 (2021).

[36] C. D. Cantwell, D. Moxey, A. Comerford, A. Bolis, G. Rocco, G. Mengaldo, D. De Grazia, S. Yakovlev, J.-E. Lombard, and D. Ekelschot, "Nektar++: An open-source spectral/*hp* element framework," Comput. Phys. Commun. **192**, 205–219 (2015).

[37] A. Wynn, D. Pearson, B. Ganapathisubramani, and P. J. Goulart, "Optimal mode decomposition for unsteady flows," J. Fluid Mech. **733**, 473–503 (2013).

[38] H. M. Blackburn and J. M. Lopez, "On three-dimensional quasiperiodic Floquet instabilities of two-dimensional bluff body wakes," Phys. Fluids **15**(8), L57–L60 (2003).

[39] L. Patruno, M. Ricci, S. de Miranda, and F. Ubertini, "Numerical simulation of a 5: 1 rectangular cylinder at non-null angles of attack," J. Wind Eng. Ind Aerodyn. **151**, 146–157 (2016).

[40] B. S. Carmo, S. J. Sherwin, P. W. Bearman, and R. H. Willden, "Wake transition in the flow around two circular cylinders in staggered arrangements," J. Fluid Mech. **597**, 1–29 (2008).

[41] D. Xin, H. Zhang, and J. Ou, "Secondary wake instability of a bridge model and its application in wake control," Comput. Fluids **160**, 108–119 (2018).

[42] M. C. Thompson, T. Leweke, and C. H. Williamson, "The physical mechanism of transition in bluff body wakes," J. Fluids Struct. **15**(3–4), 607–616 (2001).

[43] A. Naghib-Lahouti, P. Lavoie, and H. Hangan, "Wake instabilities of a blunt trailing edge profiled body at intermediate Reynolds numbers," Exp. Fluids **55**, 1779 (2014).